Dynamics of global scale electron and proton precipitation induced by a solar wind pressure pulse

M. Meurant, J.-C. Gérard, B. Hubert, V. Coumans, and C. Blockx
Laboratoire de Physique Atmosphérique et Planétaire, Université de Liège, Liège, Belgium

N. Østgaard and S. B. Mende
Space Science Laboratory, University of California, Berkeley, California, USA

Received 20 June 2003; revised 11 September 2003; accepted 16 September 2003; published 18 October 2003.

[1] On April 28 2001, simultaneous global images of electron and proton aurora were obtained by IMAGE-FUV following a sudden increase of solar wind dynamic pressure. The local time and intensity distribution of both types of precipitation are examined and compared. It is found that the electron and the proton precipitation both start in the post noon sector and expand concurrently, but the expansion into the nightside starts sooner for the protons than for the electrons. The characteristic rise time in the onset sector is on the order of 6 minutes. A distinct dynamics and morphology of electron and proton precipitation is observed in the nightside sector. DMSP electron measurements in the afternoon sector indicate that the shock has a significant effect on the electron spectral characteristics. It is suggested that the various Alfven frequencies generated by the shock account for the two different speeds of propagation of the disturbance. *INDEX TERMS:* 2154 Interplanetary Physics: Planetary bow shocks; 2407 Ionosphere: Auroral ionosphere (2704); 2704 Magnetospheric Physics: Auroral phenomena (2407). **Citation:** Meurant, M., J.-C. Gérard, B. Hubert, V. Coumans, C. Blockx, N. Østgaard, and S. B. Mende, Dynamics of global scale electron and proton precipitation induced by a solar wind pressure pulse, *Geophys. Res. Lett.*, *30*(20), 2032, doi:10.1029/2003GL018017, 2003.

1. Introduction

[2] Abrupt solar wind variations such as pressure pulses associated with CMEs can induce significant auroral precipitation [*Zhou and Tsurutani*, 1999; *Chua et al.*, 2001; *Hubert et al.*, 2003]. Possible mechanisms responsible for these shock aurora were recently discussed by *Zhou et al.* [2003]. Soon after the arrival of a solar wind pressure pulse, particles are accelerated along the compressed magnetic field lines and precipitate into the ionosphere. The first region of auroral activity is generally located in the noon sector. Within a few minutes, the region of auroral emission expands longitudinally, reaches the dawn and dusk sectors and eventually the nightside. The delay between the arrival of the shock on the front of the magnetosphere and the auroral response is shorter than the convection timescale [*Chua et al.*, 2001]. Due to the short rise time, the magnetosphere does not have time to equilibrate with the new magnetic field configuration and strong transient perturbations are observed everywhere in the magnetosphere [*Boudouridis et al.*, 2003]. The regions of the magnetosphere affected by these shocks are generally more extended than for substorms. Based on coincident POLAR UVI and DMSP measurements, *Chua et al.* [2001] determined that the mean energies of the precipitated electrons ($E_{ave} \leq$ 7 keV) are lower than those of auroral electrons during isolated substorms.

[3] In this study, we compare the dynamics of shock-induced electron and proton precipitation on April 28, 2001 in the context of the interplanetary magnetic field (IMF) measured by the Advanced Composition Explorer (ACE) satellite data. Global auroral images were collected with the FUV cameras on board the IMAGE satellite and provided simultaneous snapshots of electron and proton precipitation with a 2-minute resolution. By identification of similarities and differences between the two auroral components we put constrains on possible mechanisms causing the longitudinal extension of the precipitation away from the initial onset location.

2. The April 28, 2001 Shock Aurora

[4] The Wideband Imaging Camera (WIC) responds primarily to the N_2 LBH bands while the SI13 passband includes the OI 135.6 nm emission and nearby LBH bands [*Mende et al.*, 2000]. The SI12 imager is sensitive to Doppler-shifted Lyman-α emission at 121.8 nm generated by proton precipitation. Using simultaneous images obtained with the WIC, SI13 and SI12 imagers, it is possible to determine the spatial distribution of the precipitated electron mean energy and the electron and proton energy and number fluxes [*Meurant et al.*, 2003; *Gérard et al.*, 2001]. A correction algorithm [*Immel et al.*, 2000; *Hubert et al.*, 2003] is first applied to the WIC data to remove the dayglow contribution on the dayside.

[5] The IMAGE spacecraft was ideally located (at 7 Re geocentric distance, MLAT = 57.6°, MLT = 10.8) to observe the effects of the solar wind pressure pulse of April 28, 2001. The event took place after a long period (36 h) of quiet solar wind (SW) with a speed of 450 km/s and a weak interplanetary magnetic field (IMF) ($\sim$6 nT) (Figure 1). Before the shock, the eastward component of the solar wind velocity (V_y) was negative ($-$50 km/s), the V_z component was close to zero, the IMF B_y component was positive (6 nT) and B_z was slightly positive (+3 nT). A sudden increase of SW dynamic pressure was recorded by ACE at 0432 UT when it jumped from 0.8 to 9.6 nPa. Calculation of

0094-8276/03/2003GL018017$05.00

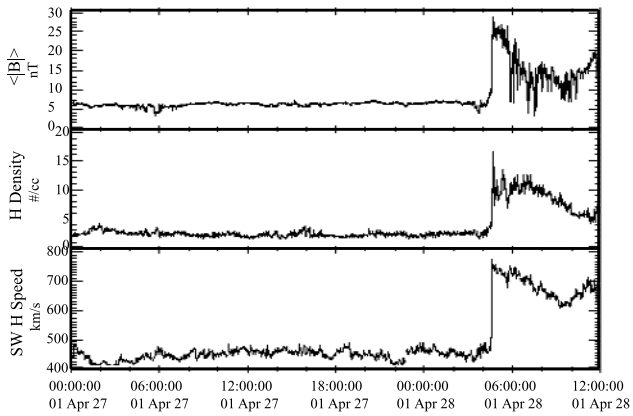

Figure 1. Solar Wind and IMF discontinuity measured by ACE before and during the precipitation observed by IMAGE.

the propagation of the disturbance to the ionosphere indicates that the shock reached the front of the magnetosphere around 0501 UT, consistent with the FUV images (Figure 2) that observed the first intensification just before 0500 UT. After the shock, the incidence of SW on the front of the magnetosphere is slightly shifted to the East (the angle with the Sun - Earth axis is 5° before and 7.5° after the shock).

[6] The first two images displayed on each panel of Figure 2 present the quiet conditions prior to the arrival of the shock. The first shock-induced precipitation was observed at 0500 UT in both the electron and proton induced emissions over a wide area in the post-noon region (11.5–15.5 MLT and 67°–81° MLAT) at exactly the same location. In the next pair of images (0502 UT), the cusp signature is observed in the post-noon sector at higher latitudes (14.3 MLT, 79° MLAT) than the initial shock-induced precipitation. The SI12 image at 0502 UT shows the dominantly eastward propagation of proton precipitation to the nightside region. The expansion of the electron precipitation is observed two minutes later (WIC image - 0504UT). The faster propagation speed of proton precipitation constitutes a first important difference compared to the electron shock induced aurora. Comparing the WIC and SI12 images at 0504 UT, 0506UT, and 0508 UT a second notable difference becomes clear: the proton precipitation appears symmetrically distributed around the noon - midnight axis whereas electron precipitation is mainly confined in the pre-midnight sector. All regions, except for a small sector near midnight, are enhanced 10 min after the shock. During this sequence, the initial intensification in the 1400 MLT region persists as the brightest region.

[7] In Figures 3a and 3b we present the different dynamics of electron and proton precipitation as MLT keograms. Each pixel of these keograms is obtained by averaging the auroral intensities between 68°–78° MLAT in MLT intervals of 30 minutes. Dayside emissions (8–16 MLT) from electrons and protons exhibit nearly the same distribution and time evolution. Both emission move away from their initial location (post-noon sector) and reach the dusk sector between 0500 UT and 0512 UT. They last ~20 minutes and disappear with a sudden and transient precipitation occur-

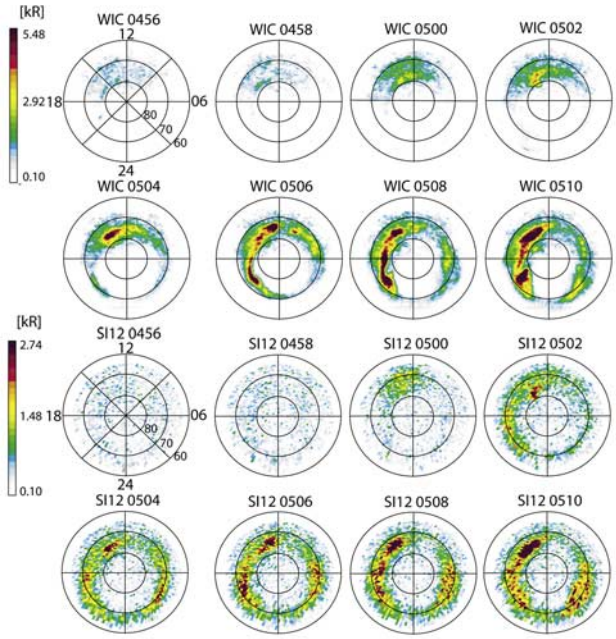

Figure 2. Sequence of WIC (top) and SI12 (bottom) images from the northern hemisphere displayed on a geomagnetic grid with local noon at the top of each image. The data were obtained between 0456 UT (5 minutes before the shock) and 0510 UT (9 minutes after the shock). The weak WIC signal on the dayside is a residual dayglow contribution not completely removed by the dayglow subtraction scheme.

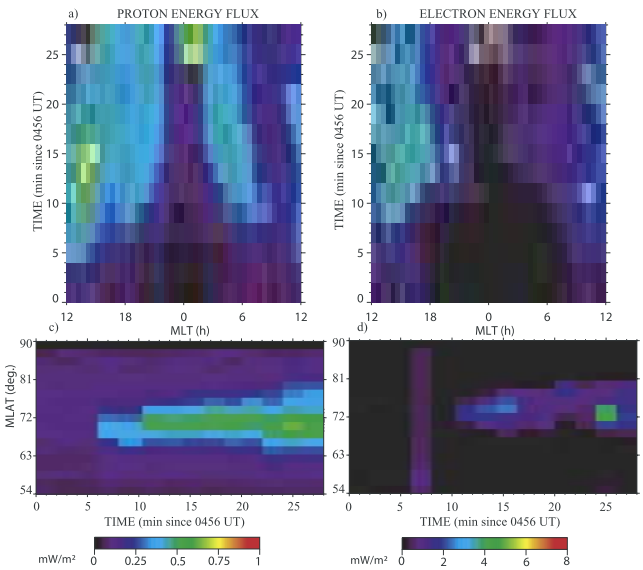

Figure 3. Expansion in time of the electron and proton precipitation away from their initial location at ~13 MLT following the increase of the solar wind pressure. (a) and (b): keograms showing the time evolution of the MLT (horizontal axis) distribution of energy flux in the 68°–78° MLAT band. (c) and (d): Time evolution of the average proton and electron energy fluxes in the 18–24 MLT sector as a function of magnetic latitude (within MLAT intervals of 2 degrees). Proton energy fluxes are displayed in the left and electron energy fluxes are displayed in the right panel.

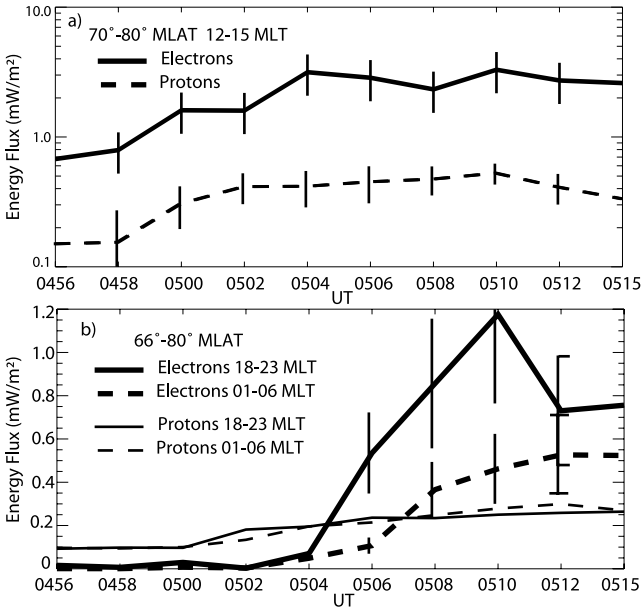

Figure 4. (a) Mean electron and proton energy fluxes in the 70°–80° MLAT, 12–15 MLT region. (b) Mean electron and proton energy fluxes in the 68°–78° MLAT band, in the 18–23 MLT sector for the pre-midnight and 01–06 MLT sector for the post-midnight region. The size of the error bars is defined by the validation of the energy flux deduction method based on IMAGE data [*Meurant et al.*, 2003].

ring around midnight and the appearance of a transpolar aurora (not shown). A similar behavior of electron precipitation was described by *Craven et al.* [1986]. During this time period, energy fluxes are higher on the dayside both for electrons (maxima are 4mW/m^2 in the dayside and 2 mW/m^2 in the nightside) and protons (0.75 mW/m^2 in the dayside; 0.4 mW/m^2 in the nightside). The electron mean energy, as deduced from the WIC/SI13 ratio, is ~5 keV on the dayside. On the nightside, however, the electron and proton precipitation appears quite different. As already exhibited by Figure 2, proton precipitation is distributed symmetrically around the noon-midnight axis while electron precipitation is mainly found in the pre-midnight region. In addition, electron nightside precipitation occurs during a shorter time (0504 to 0515 UT - 8 to 19 min after 0456 UT in Figure 3) than proton precipitation (between 0502 UT and 0521 UT - 6 to 25 min). The latitudinal motion of the peak of the electron and proton energy flux is equatorward in the post-noon region (not shown) and poleward in the pre-midnight sector (Figures 3c and 3d). The peak of proton precipitation occurs almost 3° equatorward (68° MLAT) of electrons on the nightside. By contrast, the dayside peaks of electron and proton precipitation occur at the same magnetic latitude (not shown). Both electron and proton fluxes reach their highest values on the dayside ~10 minutes after the shock.

[8] Figure 4a presents the evolution of the mean electron and proton energy fluxes in the post-noon sector (70°–80° MLAT and 12–15 MLT). It shows a parallel increase for electrons and for protons. Figure 4b presents electron and proton energy fluxes integrated over the 66°–80° MLAT band, in the 18–23 MLT and 01–06 MLT sectors. These curves confirm the asymmetry of electron precipitation about the noon-midnight meridian, whereas proton precipitation is found to be symmetric in local time. As seen from images and keograms, the nightside proton emission precedes the electrons. The maximum hemispheric total power value is 50 GW, reached 10 minutes after the shock. The energy injected during this event is estimated 3.6×10^{13} J for electrons and 1×10^{13} J for protons. Comparing these values with those derived with the same instruments during substorms, the fraction of energy carried by protons appears a factor 1.6 ± 0.3 larger during this event than during auroral substorms.

3. Discussion and Conclusion

[9] As a very quiet period preceded this event, the effects induced by the shock can be observed without any other superimposed independent process. The sequence of effects may be summarized as follows. The electron and proton onsets occurred simultaneously (within the instrumental 2-min. resolution) at the same dayside location, probably as a result of adiabatic compression of the magnetosheath by the solar wind. The pressure pulse moves the cusp signature, as seen in both the WIC and SI12 images, to higher altitudes (from 0500 UT to 0502 UT). On the dayside, the dynamics of electron and proton precipitation follow the same evolution. The characteristic risetime is on the order of 6 minutes (Figure 4a). An expansion into the dusk sector occurs during the first 10 minutes and a very low activity is observed in the pre-noon region. It is notable that, in the 1400 MLT sector, permanent electron and proton precipitation occurs during the propagation of the disturbance (between 0502 and 0510 UT). The dynamics of the two

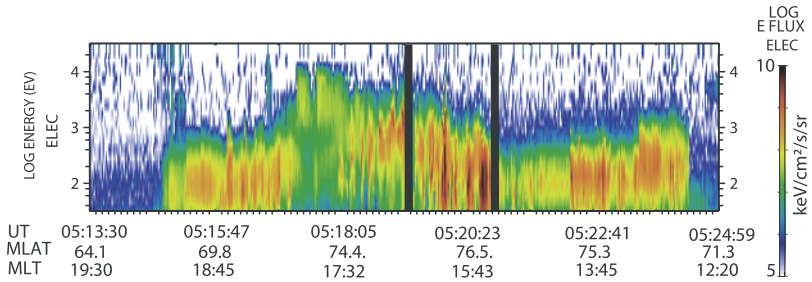

Figure 5. DMSP spectrogram of auroral electrons measured in the afternoon sector 17 minutes after the shock. The vertical marks show the region were the energy spectra are significantly different from the measurements obtained one orbit earlier.

types of precipitation are different on the nightside. Proton precipitation reaches the pre-midnight sector within 2 min following the initial dayside brightening, whereas electron precipitation appears 2 minutes later. Alfven waves generated by the bending of magnetic field lines propagate from one field line to another at speeds of the order of 1000 km/s. They reach the midnight sector in less than 2 min [*Zhou et al.*, 2003]. The sharp (but not instantaneous) increase of dynamic pressure generates various frequencies of Alfven waves. The low frequencies (supposed to be propagated faster) induced by the shock cause precipitation of particles which are not in resonance with Alfven waves before the shock. Since protons are in resonance with low frequencies (due to their lower gyro-frequencies), they are precipitated before electrons in the nightside region. This explanation assumes that the Alfven waves are generated by the shock, which is consistent with DMSP-F15 data obtained before and 17 min after the shock (Figure 5). The DMSP-F15 satellite crossed the post-noon region of auroral emission. Along the DMSP track, both DMSP and IMAGE detect only electron precipitation (not shown). During the quiet period prior to the shock (one DMSP orbit earlier), inverted V's structures were observed. After the shock, in the highest latitude regions of the post-noon sector, the inverted-V structures were replaced by electron precipitation with enhanced low energies, a typical the signature of Alfven wave acceleration as indicated by studies based on the FAST satellite measurements [*Mende et al*., 2003]. FUV imagers observed an asymmetry relative to the noon-midnight axis with a higher activity in the afternoon and evening sectors for both electron and proton. This asymmetry may be linked with the magnetospheric configuration of the negative solar wind v_y component during more than 90 minutes before the shock. In this most active region, protons are injected in the nightside region during almost the entire event (20 minutes) whereas electron precipitation is observed during only $\sim$12 minutes. The morphology of nightside emissions is significantly different, with proton precipitation at lower latitude than the electron aurora and a location of proton precipitation distributed symmetrically of the midnight - noon axis.

[10] This case study provides evidence for significant differences between electron and proton precipitation when a large pressure pulse hits the magnetosphere. Electron and proton auroral dynamics are very similar on the dayside where precipitation is likely directly triggered by adiabatic compression of the magnetic field lines. The high speed of the electron and proton aurora propagation to the nightside region suggests that these aurorae are caused by Alfven waves generated by the shock. These differences between electron and proton precipitation on the nightside can be explained by the interaction between protons and the fastest propagating low frequency Alfven waves. Future studies will define the statistical behavior of proton and electron precipitation associated with solar wind pressure pulses and examine the influence of the pre-shock conditions on the evolution the electron and proton precipitation.

[11] **Acknowledgments.** J.-C. G. is supported by the Belgian National Fund for Scientific Research (FNRS). The IMAGE-FUV investigation was supported by NASA through SWRI subcontract number 83820 at the University of California, Berkeley, contract NAS5-96020. This research was partly funded through the PRODEX program of the European Space Agency. We thanks G. Munhoven for helping with the data presentation and the IMAGE team at Berkeley. ACE level 2 data were provided by N. F. Ness (MFI) and D. J. McComas (SWEPAM), at the ACE science center.

References

Boudouridis, A., E. Zesta, and L. R. Lyons, Effect of solar wind pressure pulses on the size and strength of the auroral oval, *J. Geophys. Res.*, *108*, 8012, doi:10.1029/2002JA009373, 2003.

Chua, D., G. Parks, M. Brittnacher, W. Peria, G. Germany, J. Spann, and C. Carlson, Energy characteristics of auroral electron precipitation: A comparison of substorms and pressure pulse related auroral activity, *J. Geophys. Res.*, *106*, 5945, 2001.

Craven, J. D., L. A. Frank, C. T. Russell, E. J. Smith, and R. P. Lepping, Global auroral responses to magnetospheric compressions by shocks in the solar wind: Two case studies, in *Solar Wind-Magnetosphere Coupling*, edited by Y. Kamide and J. A. Slavin, 377–380, *Terra Scientific Publ. Co*., Tokyo, 1986.

Gérard, J.-C., B. Hubert, M. Meurant, V. I. Shematovich, D. V. Bisikalo, H. Frey, S. B. Mende, G. R. Gladstone, and C. W. Carlson, Observation of proton aurora with IMAGE FUV imager and simultaneous ion flux in situ measurements, *J. Geophys. Res.*, *106*, 28,939, 2001.

Hubert, B., J.-C. Gérard, S. A. Fuselier, and S. B. Mende, Observation of dayside subauroral proton flashes with the IMAGE-FUV imagers, *Geophys. Res. Lett.*, *30*, 1145, doi:10.1029/2002GL016464, 2003.

Immel, T. J., J. D. Craven, and A. C. Nicholas, An empirical model of the OI FUV dayglow from DE-1 images, *J. Atmos. Solar-Terr. Phys.*, *62*, 47, 2000.

Mende, S. B., C. W. Carlson, H. U. Frey, T. J. Immel, and J.-C. Gérard, IMAGE FUV and in situ FAST particle observations of substorm aurorae, *J. Geophys. Res.*, *108*(A4), 8010, doi:10.1029/2002JA009413, 2003.

Mende, S. B., et al., Far ultraviolet imaging from the IMAGE spacecraft, 1, System design, *Space Sci. Rev.*, *91*, 243, 2000.

Meurant, M., J. C. Gérard, B. Hubert, V. Coumans, V. I. Shematovich, D. V. Bisikalo, D. S. Evans, G. R. Gladstone, and S. B. Mende, Characterization and dynamics of the auroral electron precipitation during substorms deduced from IMAGE-FUV, *J. Geophys. Res.*, *108*(A6), 1247, doi:10.1029/2002JA009685, 2003.

Zhou, X.-Y., R. J. Strangeway, P. C. Anderson, D. G. Sibeck, B. T. Tsurutani, G. Haerendel, H. U. Frey, and J. K. Arballo, Shock aurora, FAST and DMSP observations, *J. Geophys. Res.*, *108*, 8019, doi:10.1029/2002JA009701, 2003.

Zhou, X.-Y., and B. T. Tsurutani, Rapid intensification and propagation of the dayside aurora: Large scale interplanetary pressure pulses (fast shocks), *Geophys. Res. Lett.*, *26*, 1097, 1999.

M. Meurant, J.-C. Gérard, B. Hubert, V. Coumans, and C. Blockx, Laboratoire de Physique Atmosphérique et Planétaire, Université de Liège, Allée du 6 Aout, 17, Bat. B5C, Belgium. (mmeurant@ulg.ac.be)

N. Østgaard and S. B. Mende, Space Science Laboratory, University of California, 7 Gauss Way, Berkeley, CA 94720, USA.